

EMBEDDED, SELF-GRAVITATING EQUILIBRIA IN SHEETLIKE AND FILAMENTARY MOLECULAR CLOUDS

CHARLES L. CURRY¹

Department of Physics, University of Waterloo, Waterloo, ON N2L 3G1

and

Department of Physics and Astronomy, University of Western Ontario, London, ON N6A 3K7

TO APPEAR IN APJ: OCT 1, 2000

ABSTRACT

Numerical solutions of the isothermal Lane-Emden equation are presented, corresponding to self-gravitating gaseous cores embedded within a finite density envelope of overall cylindrical symmetry. These structures may be members of a fragmentation hierarchy proceeding from sheets, to filaments, to elongated, prolate clumps. The embedded solutions are the first of their kind, and as such represent a significant improvement upon the isolated cloud paradigm used almost exclusively by previous authors. The properties of the equilibria are in reasonable agreement with observations of dense molecular cores in star-forming clouds, despite the fact that there is only one free parameter in the models. We show that this parameter may be identified with the critical wavelength for instability in the parent filament. The implications of further fragmentation and the possible influence of magnetic fields are briefly discussed.

Subject headings: ISM: clouds — ISM: structure — hydrodynamics — instabilities — Stars: formation

1. INTRODUCTION

The present observational picture of star-forming regions conveys cloud structures considerably more varied than any one theoretical scenario can explain. Nevertheless, there are certain points of correspondence, when one restricts attention to the molecular, self-gravitating component of the interstellar medium. On scales of tens to hundreds of parsecs, both atomic and molecular gas clouds appear shell-like and filamentary (Scalo 1985; Kulkarni & Heiles 1988). Shells may be formed by several distinct dynamical processes: cloud-cloud collisions (Smith 1980), compressional shock waves from supernovae or OB stars (McCray & Kafatos 1987), and large-scale shocks associated with spiral density waves (Roberts 1969) are but a few possibilities. Filamentary structure persists down to scales of several parsecs, to the regime of individual molecular clouds [Loren 1989, Nozawa et al 1991 (ρ Oph); Heyer et al 1987, Onishi et al 1996 (Taurus); Bally et al 1987, Tatematsu et al 1993 (Orion)]. Each filament typically contains several distinct sub-condensations in close proximity to each other, some of which harbor infrared continuum sources (Onishi et al 1998). In some cases, the embedded clumps are spaced quite regularly along the filament (Schneider & Elmegreen 1979; Dutrey et al 1991). Thus, several authors have speculated that the formation of star-forming clumps proceeds via a hierarchical fragmentation process, in which filaments are formed out of larger structures, and then clumps out of the filaments (Schneider & Elmegreen 1979; Gaida, Ungerechts, & Winnewisser 1984; Hanawa et al 1993; Fiege & Pudritz 2000a).

Focusing now on the cores themselves, maps in dense tracers such as NH₃ and CS display roughly elliptical intensity contours, with a mean apparent major-to-minor axis ratio of around 2 (Jijina, Myers, & Adams 1999). Statistical arguments applied to the distribution of measured axial ratios for several surveys have prompted some authors to conclude that the cores

are more likely to be intrinsically prolate than oblate (David & Verschueren 1987; Myers et al 1991; Ryden 1996). Other statistical arguments imply that the observed elongation is unlikely to be a result of star formation or outflows (Myers et al 1991). Coupled with the additional result that the majority of cores are near virial equilibrium (Jijina et al 1999), this argues against a wholly dynamical origin for prolateness, since the implied lifetimes are then so short that observations of cores without embedded stars would be exceedingly rare (the latter represent about one-half of the ammonia cores detected in the Taurus region, and a somewhat smaller fraction in Ophiuchus and Orion). Rather, it appears more likely that cores are at least quasi-equilibrium structures, and that their shapes therefore offer some clue to the forces responsible for their formation.

If this reasoning is correct, then it leads to a formidable crisis in our current theoretical picture of cloud equilibria, which typically envisions star forming cores as self-gravitating clumps bounded by a zero density, constant pressure—and so high temperature—medium (e.g., McKee et al 1993). That is, it is difficult to conceive of prolate, quasi-equilibrium, gaseous cores as purely *isolated* structures. Non-gravitational forces, such as rotation or magnetic fields, are not likely to aid in maintaining prolate equilibria, although their role in oblate structures has been made abundantly clear.² The absence in the literature of even a single, physically acceptable, gaseous, prolate equilibrium solution suggests that a fresh theoretical approach is necessary. We examine a scenario in this paper whereby core morphology is directly attributable to a fragmentation process. As we show in §2 and 3, the existence of prolate structures within cylindrical filaments may be understood in exactly the same way as the existence of the filaments themselves: as a result of the fragmentation of the parent cloud and nonlinear growth of the fragments. What has apparently escaped attention until now, and what we demonstrate explicitly, is that *accessi-*

¹Email: curry@astro.uwo.ca

²It is in fact possible to construct isolated, prolate magnetic clouds, but these possess magnetic field structures which are highly unusual and, in any case, lack direct observational justification. See Fiege & Pudritz (2000b) and Curry & Stahler (2000) for examples.

ble, long-lived states exist wherein cores and their extensive filamentary envelopes occupy the same hydrostatic structure. We now proceed to outline a particular fragmentation hierarchy that might be responsible for such structures.

2. NONLINEAR FRAGMENTATION OF AN ISOTHERMAL LAYER

To motivate the new solutions presented in the following section, we begin by outlining a possible formation mechanism for filamentary structures in the molecular interstellar medium. By drawing attention to selected existing results in the literature, we hope to provide a more compelling argument for a particular fragmentation hierarchy alluded to previously by several authors, notably Schneider & Elmegreen (1979) and Larson (1985).

2.1. Analytic Solutions

While not realistic in detail, a large, shell-like structure in the interstellar medium may be approximated on sufficiently small scales by a planar, self-gravitating layer, or “sheet” (Elmegreen & Elmegreen 1978). We restrict consideration throughout to an isothermal, self-gravitating gas, whose equilibrium is governed by the Lane-Emden equation,

$$\nabla^2 \psi = \frac{\partial^2 \psi}{\partial x^2} + \frac{\partial^2 \psi}{\partial y^2} + \frac{\partial^2 \psi}{\partial z^2} = 4\pi G \rho_{0,s} e^{-\psi/a^2}, \quad (1)$$

where ψ is the gravitational potential, a is the constant sound speed, and $\rho_{0,s}$ is a constant. The equation has been written in cartesian coordinates (x, y, z) . When ψ varies solely in the y -direction, i.e. $\psi = \psi_{1D}(y)$, and under the usual boundary conditions $\psi_{1D}(y=0) = 0$, $(d\psi_{1D}/dy)_{y=0} = 0$, an exact solution is known (Spitzer 1942):

$$\rho_{1D}(y) = \rho_{0,s} \exp[-\psi_{1D}(y)/a^2] = \rho_{0,s} \operatorname{sech}^2(y/\ell_0), \quad (2)$$

where the scale height ℓ_0 is defined by $\ell_0 \equiv a/(2\pi G \rho_{0,s})^{1/2}$. The layer is unbounded in the y -direction; solutions truncated by an external pressure at constant y may also be constructed (e.g., Elmegreen & Elmegreen 1978). However, as these introduce an additional parameter—namely, the external pressure—into the problem, we do not consider them here. The stability of the unbounded solution was examined by Ledoux (1951), who found gravitational instability for infinitesimal sinusoidal perturbations of wavelength exceeding $\lambda_{x,cr} = 2\pi\ell_0$. The maximum growth rate occurs at $\lambda_{x,MGR} = 2.24\lambda_{x,cr} = 14.1\ell_0$. The choice of the x -direction for the perturbation wavevector here is arbitrary; the same results hold for perturbations in the z -direction only.

Subsequently, Schmid-Burgk (1967) (hereafter S-B) presented a remarkable *two-dimensional* (2D) solution of equation (1) (independently discovered, in a hydrodynamic context, by Stuart 1967):

$$\rho_{2D}(x, y) = \rho_{0,s} \exp\left[\frac{-\psi_{2D}(x, y)}{a^2}\right] = \frac{\rho_{0,s} (1-A^2)}{[\cosh(y/\ell_0) - A \cos(x/\ell_0)]^2}. \quad (3)$$

The constant A , $0 < A < 1$ describes the amplitude of spatially periodic variations along one direction parallel to the layer (here chosen as x), with the same critical wavelength, $\lambda_{x,cr}$, as found by Ledoux. As noted by S-B, this result shows that the latter

³Note also that, like other solutions of the Lane-Emden equation, S-B’s solution is homology invariant (Chandrasekhar 1958); i.e. the potential $\psi_{2D}^* \equiv \psi_{2D}(Cx, Cy) - 2 \log C$, $C = \text{constant}$, is also a solution of equation (1).

⁴The term “equilibrium” is used here in its strictly limited sense: i.e., a particular equilibrium may be either stable or unstable to perturbations in a direction in which the solution is translation-invariant (in this case, the z -direction).

mode is not restricted to infinitesimal amplitudes. Indeed, solutions of *all* amplitudes A are contained in equation (3).³ It is noteworthy that the periodicity of this exact, nonlinear solution does not correspond to that of the fastest-growing mode in the linearly unstable layer, but rather to the *critically* unstable mode. This feature is discussed further in §6.

As $A \rightarrow 0$, equation (3) reduces to Spitzer’s solution. In the limit $A \rightarrow 1$, the equilibrium⁴ corresponds to a series of parallel cylindrical “fragments,” infinitely extended in the z -direction, with density maxima separated by a distance $\lambda_{x,cr}$. For general A , the fragments are embedded, nearly elliptical cylinders with equidensity contours of eccentricity $(1-A)^{1/2}$ (see Figure 1 of S-B). The density maxima and minima along the x -axis (each spaced at an interval of $\Delta x = 2\pi\ell_0$), are given by

$$\rho_c = \rho_{0,s} \left(\frac{1+A}{1-A}\right) \quad \text{and} \quad \rho_s = \rho_{0,s} \left(\frac{1-A}{1+A}\right), \quad (4)$$

respectively.

2.2. Numerical Solution

There is reason to suspect that analogues of the S-B solution exist in other geometries, in particular in cylindrical symmetry, a case we shall focus on in the following section. Unfortunately, to our knowledge, no other embedded solutions are known in analytic form. However, numerical techniques can be used. As a test of one such scheme used later in this paper, we attempted to find the S-B solution using the self-consistent field method (e.g. Tassoul 1978). That is, equation (1) was solved iteratively on a two-dimensional grid, subject to the boundary conditions

$$\left.\frac{\partial \psi'}{\partial x'}\right|_{x'=0} = \left.\frac{\partial \psi'}{\partial y'}\right|_{y'=0} = 0, \quad (5)$$

$$\psi'(0, 0) = -\ln \rho'(0, 0), \quad \text{and} \quad \left.\frac{\partial \psi'}{\partial x'}\right|_{x'=X'} = 0. \quad (6)$$

Here a prime indicates a dimensionless quantity—e.g., $\psi' \equiv \psi/a^2$ —and $0 \leq x' \leq X'$, $0 \leq y' \leq Y'$ is the extent of the computational region. The nondimensionalization of length will be discussed below; for now it may be assumed arbitrary.

The first of conditions (5) ensures that the x -component of the gravitational field vanishes on the y -axis, while the second imposes reflection symmetry about the $x = 0$ plane. Conditions (6) are consistent with the Spitzer solution, although neither constrains the numerical solution to be identical to the former in any particular limit. In addition, these conditions allow for solutions with a periodic structure in x . In an attempt to find these, we took $\psi'_{1D,0}(y') = -\ln \rho'_{1D,0}(y')$ (see eq. 2) as an initial guess, and added a perturbation of the form

$$\delta \psi'(x', y') = \epsilon \cos(px'/X') \sin(py'/Y'),$$

where ϵ is a small, constant amplitude and $0 < p < 2\pi$. For convergence of the numerical code we required $1 - \psi'^{(n)}/\psi'^{(n+1)} < \delta = 0.005$, where $\psi'^{(n)}$ is the value of ψ' at the n^{th} iteration. For $\epsilon \lesssim 0.005$, the method converged immediately to the Spitzer solution (2). For any larger ϵ , however, a unique, 2D structure resulted. The equilibria so obtained constitute a family of

solutions in the single parameter X' , such that the density contrast ρ_c/ρ_s increases monotonically with increasing X' . Here $\rho_s \equiv \rho(X, 0)$. The vertical extent Y' was chosen sufficiently large that the effect of different Y' on 2D solutions of the same X' was negligible.

In order to compare these solutions to the analytic one of S-B, we need to specify the nondimensionalization. This is, in fact, already implicit in the solution method. At each iteration, the Lane-Emden equation is solved for $\psi'(x', y')$ with the source term

$$\rho'^{(n)}(x', y') = \exp[\psi'^{(n)}(0, 0) - \psi'^{(n)}(x', y')].$$

Thus, $\rho'(x', y')$ is normalized with respect to its *central* value at each iteration; i.e. $\rho'^{(n)}(0, 0) = 1$ (this is made explicit in the first of equations 6). Consequently, once an exact, 2D equilibrium is found, all “memory” of the original density scale $\rho_{0,s}$ is lost. The characteristic density of the solution is $\rho_c = \rho(0, 0)$, and thus the corresponding unit length is $\ell_c \equiv a/(2\pi G\rho_c)^{1/2}$, not $\ell_0 \propto \rho_{0,s}^{-1/2}$ as in the analytic solution. Hence, the appropriate nondimensionalization is specified a posteriori as

$$(x', y', z') \equiv (x/\ell_c, y/\ell_c, z/\ell_c). \quad (7)$$

An exact relation between the parameter X' in the numerical problem, and the amplitude A in the analytic solution, may now be derived.⁵ Solving equation (3) for $\psi_{2D}(x, y)$ and substituting the result into the second of equations (6) gives

$$X' = \frac{X}{\ell_c} = \pi \left(\frac{\rho_c}{\rho_s} \right)^{1/4} = \pi \left(\frac{1+A}{1-A} \right)^{1/2}. \quad (8)$$

The parameter X' represents one-half of the spacing between the embedded fragments; i.e., $\lambda'_x = 2X'$. In the analytic solution, the spacing of the fragments is constant, i.e. $\Delta x/\ell_0 = \lambda_{x,cr}/\ell_0 = 2\pi$. There the fragment spacing stays the same while the amplitude A varies. Just as analytic solutions exist for all A , numerical solutions exist for all values of $X' > \pi$.

Figure 1 of S-B (1967) shows a solution with $A = 0.17$, whose corresponding density contrast is $\rho_c/\rho_s = 1.987$. Inserting this A into equation (8), one finds $X' = 3.730$. Using this X' as input for the numerical method then yields a solution with $\rho_c/\rho_s = 1.981$, a difference of 0.3 percent from S-B’s analytic result. This solution is displayed in Figure 1. The discrepancy between the analytic and numerical solutions remains small as X' increases above 3.73, and is still less than 1 percent for $X' = 22$, $\rho_c/\rho_s \approx 2400$. At smaller X' , the numerical and analytic results slowly diverge, with the relative error in ρ_c/ρ_s reaching 5 percent at $X' = 3.32$, and nearly 20 percent at $X' = \pi$. At the latter value, equation (8) predicts $A = 0$ and $\rho_c/\rho_s = 1$. Presumably, the method is not sufficiently sensitive to the slight density contrasts present in these small amplitude ($A \lesssim 0.05$) solutions to render an accurate result. On the other hand, for $X' < 3.125$, the numerical method converges to the Spitzer solution, with a slightly non-uniform density along the midplane (e.g., $\rho_c/\rho_s \simeq 0.99$ at $X' = 3.12$). Overall, these results confirm the validity of the numerical method, with the nondimensional length and density chosen as in equation (7). We may expect the same to be true for other solutions found by the same technique, irrespective of whether an analytic solution is known.

⁵I thank Dean McLaughlin for pointing out a simplified derivation.

⁶In the S-B solution, the total mass per unit z -length of each “cell”, $-\pi \leq x/l_0 \leq \pi$, is also $2a^2/G$.

We conclude our discussion of the S-B solution by noting that related states have in fact appeared in the literature, in the context of either linear perturbation theory (Miyama, Narita, & Hayashi 1987a) or time-dependent nonlinear calculations (Miyama, Narita, & Hayashi 1987b). The basic character of the solution persists even in the presence of a (z -independent) magnetic field (Fleischer 1998; Nagai, Inutsuka, & Miyama 1998), or when the layer is truncated by an external medium. The pressure-bounded, magnetized layer has additional modes of fragmentation available to it, as shown by Nagai et al (1998). However, the significance of the basic result—namely, that the embedded filaments are in fact *exact, equilibrium solutions*—is rarely emphasized.

3. NONLINEAR FRAGMENTATION OF AN ISOTHERMAL FILAMENT

3.1. Equilibrium and Stability

In cylindrical coordinates (r, ϕ, z) , the isothermal Lane-Emden equation reads

$$\nabla^2 \psi = \frac{1}{r} \frac{\partial}{\partial r} \left(r \frac{\partial \psi}{\partial r} \right) + \frac{\partial^2 \psi}{\partial z^2} = 4\pi G \rho_{0,f} e^{-\psi/a^2}, \quad (9)$$

where $\rho_{0,f}$ is a constant. Here the z -axis is taken to coincide with the principal axis of the cylinder, and we have taken $\partial/\partial\phi = 0$, restricting consideration to axisymmetric solutions. When ψ depends only on r , i.e. $\psi = \psi_{1D}(r)$, and under the boundary conditions $\psi_{1D}(r=0) = 0$, $(d\psi_{1D}/dr)_{r=0} = 0$, Stodolkiewicz (1963) and Ostriker (1964) derived the following exact solution of equation (9) (hereafter the S-O solution):

$$\rho_{1D}(r) = \rho_{0,f} \exp \left[\frac{-\psi_{1D}(r)}{a^2} \right] = \frac{\rho_{0,f}}{(1+r^2/l_0^2)^2}, \quad (10)$$

where $l_0 \equiv (2a^2/\pi G\rho_{0,f})^{1/2}$ is the cylindrical scale radius. Interestingly, solution (10) reduces to that of S-B as $A \rightarrow 1$ in the latter; details may be found in the Appendix. This suggests that equilibria quite similar to the S-O solution may result directly from the fragmentation of an isothermal layer.

The solution (10) decreases as r^{-4} at large r ; as in the planar case, solutions truncated by an external pressure at constant r have also been considered (e.g., Inutsuka & Miyama 1997; Fiege & Pudritz 2000a). The maximum mass per unit length of the filament described by equation (10) is⁶

$$\mu_{\max} \equiv \int_0^\infty 2\pi \rho_{1D}(r) r dr = \frac{2a^2}{G}. \quad (11)$$

Isothermal cylinders with density distributions having $\mu > \mu_{\max}$ are unstable to radial collapse, while those with $\mu < \mu_{\max}$ expand radially outward, unless confined by an external pressure (e.g., Inutsuka & Miyama 1992). The stability of solution (10) to axisymmetric, linear perturbations was examined by Stodolkiewicz (1963), who found instability for perturbations of wavelength exceeding $\lambda_{z,cr} = 3.94 l_0$. The maximum growth rate occurs at $\lambda_{z,MGR} = 1.98 \lambda_{z,cr} = 7.82 l_0$ (Nagasawa 1987). Further analysis has been carried out by Inutsuka & Miyama (1997) in the nonlinear regime of perturbation growth. However, the nonlinear *resolution* of the instability remains an open question. That is, what is the final outcome of the fragmentation instability in an isothermal cylinder?

3.2. Numerical Solution

We undertake a numerical investigation of the question posed above, using an identical technique to that described in §2.2. That is, rather than following the time evolution of a particular unstable state, we instead search for an exact, static solution having a 2D structure. The boundary conditions on the potential are now

$$\left. \frac{\partial \psi'}{\partial r'} \right|_{r'=0} = \left. \frac{\partial \psi'}{\partial z'} \right|_{z'=0} = 0, \quad (12)$$

$$\psi'(0,0) = -\ln \rho'(0,0), \quad \text{and} \quad \left. \frac{\partial \psi'}{\partial z'} \right|_{z'=Z'} = 0, \quad (13)$$

where $0 \leq r' \leq R'$, $0 \leq z' \leq Z'$ is the size of the computational region. The nondimensionalization is the same as that used in §2.2, except with ℓ_c replaced by $l_c \equiv (2a^2/\pi G \rho_c)^{1/2}$, where $\rho_c \equiv \rho(0,0)$. Again we took the equilibrium potential, $\psi'_{1D}(r') = -\ln \rho'_{1D}(r')$ as an initial guess, and added a perturbation of the form

$$\delta \psi'(r', z') = \epsilon \sin(pr'/R') \cos(pz'/Z'),$$

with $0 < p < 2\pi$. For any $\epsilon \gtrsim 0.005$, a family of unique 2D structures was again found, now parameterized by Z' . The corresponding R' was chosen sufficiently large that its effect on the solutions was negligible. In practice, choosing R' to be approximately twice the radius of the “tidal lobe”—i.e., the last closed isodensity contour, of density $\rho_s \equiv \rho(0, Z')$ —was sufficient.

The density contrast between the center and the tidal lobe, ρ_c/ρ_s , is a monotonically increasing function of Z' . Models with $1.2 < \rho_c/\rho_s \lesssim 10^3$ were generated, corresponding to $2.1 < Z' \leq 30$. A few representative equilibria are displayed in Figure 2. At small Z' , the equidensity contours are highly prolate (Fig. 2a); as Z' increases, the interior contours become nearly spherical (Fig. 2d). Note that we were able to find 2D equilibria only down to a minimum $Z' \simeq 2.1$; below this value, convergence was not obtained until $Z' = 1.8$. For all $Z' \leq 1.8$, the method converged to the S-O solution, with a slightly non-uniform density along the axis of symmetry (e.g., $\rho_c/\rho_s = 0.997$ at $Z' = 1.8$). As we discuss below in §6, these results strongly suggest a fragmentation scale $\simeq \lambda_{cr}$, as in the planar layer.

Physically, the quantity $2Z'$ may be interpreted as the separation between any two clumps in a linear chain of identical condensations (e.g. Lizano & Shu 1989; Fiedler & Mouschovias 1992). This feature thus mimics an observed property of star-forming environments: namely, that pre-stellar cores are rarely found in isolation. In §4.2, we examine how the properties of the condensations depend upon Z' , and how the latter may be constrained by observations.

4. PHYSICAL PROPERTIES OF THE FRAGMENTS

4.1. Virial Theorem Analysis

Insight into the global properties of equilibria may be obtained from the scalar virial theorem. In the present context of embedded cores, however, care must be taken regarding the region of application. For an axisymmetric cloud in equilibrium, we have (McKee et al 1993)

$$2U + \Pi + W = 0, \quad (14)$$

where

$$U = \frac{3}{2} \int_V P dV = \frac{3}{2} a^2 M,$$

$$\Pi = - \int_S P \mathbf{r} \cdot d\mathbf{S},$$

and

$$W = - \int_V \rho \mathbf{r} \cdot \nabla \psi dV$$

are the relevant thermal, compressive, and gravitational energies. These integral quantities are usually summed over the volume V enclosed within an arbitrary closed surface S . In the present case, one might choose for S any closed isobar. Then the thermal and compressive terms are easily calculated. However, for any choice of S the gravitational energy W is incomplete because part of the gravitational field arises from *outside* the region considered. This is in keeping with the nature of embedded equilibria. Indeed, each equilibrium found by the numerical method of the previous section comprises an entire “cell,” i.e., the region $0 \leq r \leq R$, $0 \leq \phi \leq 2\pi$, $-Z \leq z \leq Z$, so that the above choice of S is inappropriate in any case. The virial theorem may only be consistently applied on the same region. Since the gravitational force vanishes on the plane circular section $z = \pm Z$ (by the second of the boundary conditions eq. 13), the corresponding energy W summed over the entire cell between $z = -Z$ and $z = +Z$ is therefore complete.

Figure 3 shows the behavior of individual terms in the virial equation (14), expressed in dimensionless units, along with their sum, $\Sigma \equiv 2U + \Pi + W$, as one proceeds along a sequence of increasing central density ρ_c/ρ_s . Here, ρ_s is used as a convenient reference density only; the virial terms have been calculated for the entire cell, not just for the region inside the tidal lobe. The figure shows that the compressive term Π has a magnitude of only 40 to 50 percent of the gravitational term W over most of the sequence. This may be compared with the case of isolated clouds, where external compression exceeds the effect of self-gravity at low density contrast, the latter becoming dominant only for more centrally-condensed clouds. There, the boundary pressure is all that prevents the cloud from dispersing. That there are no such equilibria in the present sequence can also be seen by considering the total energy, $E \equiv W + U$, also plotted in Fig. 3. Since $E < 0$ for all ρ_c/ρ_s , *all of the equilibria are gravitationally dominated*. Indeed, this feature is consistent with the notion that such structures are the result of nonlinear fragmentation within the self-gravitating parent filament. Note that this also means that the prolate shape of the cores is *not* primarily due to tidal stretching by adjacent cores; an effect that, in the isolated case, may be mimicked by use of the boundary condition eq. (13) (see, e.g., Curry & Stahler 2000). Finally, note that all three of U , Π and W approach nonzero limiting values as $\rho_c/\rho_s \rightarrow 1$. This is to be expected, since these quantities are nonzero in the S-O cylinder. Their limiting values are readily calculated as: $U_0 = 3\pi Z'$, $\Pi_0 = -2\pi Z'$, and $W_0 = -4\pi Z'$.

4.2. A Sequence of Prolate Equilibria

As indicated by the dashed curves in Fig. 2, for a given Z' there exists a unique tidal lobe, within which the equidensity contours are closed, and that corresponds to a density minimum along the symmetry axis, $r = 0$. The intersection of the tidal lobe and the $z = 0$ plane is a circle whose radius we denote by R_t . The tidal lobe is thus one possible definition of the “surface” of the dense core, since it marks where the latter may be distinguished from the background filament. However, these

solutions make clear the danger of taking such a term too literally. On this interpretation, we may fix the density on the tidal lobe at a value appropriate to the intercore medium. (Defining the extent of a core using a single equidensity contour is in fact in accord with the usual observational definition, which assigns a core's size on the basis of its associated half-power intensity contour).

Fixing the intercore density $\rho_s = \bar{m}n_s$ and temperature T allows one to characterize the size and mass of the fragments via the following reference quantities:

$$l_s \equiv \left(\frac{a^2}{G\rho_s} \right)^{1/2} = \left(\frac{\pi \rho_c}{2 \rho_s} \right)^{1/2} l_c, \quad m_s \equiv \rho_s l_s^3 = \frac{a^3}{(G^3 \rho_s)^{1/2}}. \quad (15)$$

In terms of these reference values, we now define the dimensionless lengths and mass:

$$\tilde{Z} \equiv \frac{Z}{l_s} = Z' \left(\frac{\pi \rho_c}{2 \rho_s} \right)^{-1/2}, \quad \tilde{R}_t \equiv \frac{R_t}{l_s}, \quad \text{and} \quad \tilde{M}_t \equiv \frac{M_t}{m_s}, \quad (16)$$

where M_t is the dimensional mass contained within the tidal lobe.

Figure 4 shows the behavior of \tilde{Z} , \tilde{R}_t , and \tilde{M}_t as a function of density contrast for fixed a and n_s . The results are reminiscent of the Bonnor-Ebert (hereafter B-E) sequence, shown by dashed lines, but with a maximum in mass at $\rho_c/\rho_s \simeq 10.0$ instead of at $(\rho_c/\rho_s)_{\text{BE}} = 14.04$. The maximum mass of the prolate sequence, $\tilde{M}_t = 1.32$, exceeds that of the B-E sequence, $\tilde{M}_{\text{BE}} = 1.182$ by 12 percent. The polar radius \tilde{Z} decreases from a value of 1.53 at $\rho_c/\rho_s \simeq 1.2$ to a minimum of 0.60 at $\rho_c/\rho_s \simeq 600$. The tidal lobe radius \tilde{R}_t has a maximum of 0.45 at $\rho_c/\rho_s \simeq 6.4$, and a minimum of 0.34 at $\rho_c/\rho_s \simeq 10^3$.

Finally, it is instructive to compare the density structure of the prolate fragments with that of known equilibria. The equatorial and polar density profiles for the models displayed in Figs. 2c and d are shown in Figures 5a and b. These figures also show the radial density profiles of a S-O cylinder and of a marginally stable B-E sphere. At the relatively low ρ_c/ρ_s of Fig. 5a, the polar density profile is shallower than z^{-2} , while the equatorial density resembles that of a B-E sphere out to about three times its ‘‘core radius,’’ after which it steepens to the r^{-4} of the S-O profile. At high ρ_c/ρ_s (Fig. 5b), the similarity of both density profiles to that of the B-E sphere is evident. Thus, except at very low central concentrations or at distances far outside the tidal lobe, the core's density structure bears little resemblance to that of its parent S-O cylinder. This is consistent with observations of globular filaments, which rarely imply density profiles steeper than r^{-2} (Alves et al 1998; Johnstone & Bally 1999; Lada, Alves, & Lada 1999).

4.3. Remarks on Stability

In the case of isolated, pressure-bounded clouds, the presence of a maximum in cloud mass as one proceeds from smaller to larger ρ_c/ρ_s signifies a transition from stable to unstable equilibria. However, this technique (often referred to as the ‘‘static method’’; Tassoul 1978), cannot be carried over to the embedded cores characterized by the mass \tilde{M}_t , since they are not complete equilibria (§4.1). Thus, the maximum in the \tilde{M}_t vs. ρ_c/ρ_s relation seen in Fig. 4, while suggestive, has no direct bearing on the issue of stability.

Another method used to investigate the stability of isolated clouds is that of the Gibbs free energy (Stahler 1983; Tomisaka

et al 1988). Unfortunately, this method is also unlikely to succeed here, for the following reason. Along a sequence of equilibria of fixed temperature and surface pressure, the Gibbs free energy is a minimum at the critical stability point. However, in the present context, an equilibrium consists of an entire cell, which lacks a single, isobaric bounding surface. It is therefore impossible to construct a sequence of cells of fixed a and n_s , for which quantities such as mass have definite maxima. Consequently, one finds that the Gibbs free energy is a monotonically decreasing function of ρ_c/ρ_s ; i.e., no minimum value is attained along the sequence. Thus, the free energy approach cannot be applied in the usual manner. Explicit, time-dependent calculations of the evolution of small perturbations within the equilibria may be required to illuminate this important issue.

5. COMPARISON WITH OBSERVATIONS

To compare with observations, it is useful to write l_s and m_s as

$$l_s = 0.382 \text{ pc} \left(\frac{a}{0.19 \text{ km s}^{-1}} \right) \left(\frac{n_s}{10^3 \text{ cm}^{-3}} \right)^{-1/2}, \quad (17)$$

$$m_s = 3.19 M_\odot \left(\frac{a}{0.19 \text{ km s}^{-1}} \right)^3 \left(\frac{n_s}{10^3 \text{ cm}^{-3}} \right)^{-1/2}. \quad (18)$$

The scaling for n_s is the minimum total number density, $n = 1.2n_{\text{H}_2}$, estimated from ^{13}CO measurements of filamentary clouds (Nercessian et al 1988), while that for a is the thermal sound speed for $T = 10 \text{ K}$ and a mean molecular weight of $\bar{m} = 2.33 m_{\text{H}}$. In a high mass star-forming region such as Orion, n_s can be as high as $\sim 10^4 \text{ cm}^{-3}$ (Dutrey et al 1993), while $a \propto T^{1/2}$ can exceed 0.40 km s^{-1} . Nonthermal motions, which dominate thermal motions in clouds above scales $\sim \text{few} \times 0.1 \text{ pc}$, may be included in a schematic manner by replacing a with a constant velocity dispersion σ . Representative values of σ are given below.

With the above scalings, the results of Fig. 4 correspond to the following ranges:

$$\begin{aligned} 0 < M/M_\odot &\leq 4.2, \\ 0.23 \text{ pc} &\leq Z \leq 0.58 \text{ pc}, \\ 0 &\leq R_t \leq 0.17 \text{ pc}. \end{aligned}$$

These ranges are in reasonable agreement with deduced values for cores observed in dense tracers, such as ammonia (Jijina et al 1999). This is true even though NH_3 has a critical excitation density, $n_{\text{ex}} \sim 10^4 \text{ cm}^{-3}$, an order of magnitude larger than our assumed n_s . However, this effect is offset in equations (17) and (18) by the fact that some regions have $T > 10 \text{ K}$ and that all exhibit nonthermal motions.

We now compare the intercore separations found in this simple model with those observed in star-forming regions. Two values of \tilde{Z} may be singled out from Fig. 4 as being of particular interest. The first, denoted by \tilde{Z}_{peak} , corresponds to the peak in \tilde{M}_t , and has the value $\tilde{Z}_{\text{peak}} = 0.94$. The second notable value is the minimum in \tilde{Z} occurring near the right-hand side of Fig. 4, $\tilde{Z}_{\text{min}} = 0.60$. The dimensional value of each of these quantities depends upon both the intercore density and velocity dispersion through equations (16) and (17). Figure 6 shows both characteristic separations as a function of n_s for various σ , where the latter is given in terms of $a_{10} \equiv 0.19 \text{ km s}^{-1}$, the thermal sound speed in $T = 10 \text{ K}$ gas. The range of observed intercore separations, $2Z_{\text{obs}}$, in each of three star-forming regions—Taurus,

Ophiuchus, and Orion—is indicated by vertical bars on the graph. These ranges were deduced from molecular line maps of cores embedded within filaments in each region. The characteristic intercore density was estimated as the observed density at a scale corresponding to the mean value of $2Z_{\text{obs}}$ for that region. Further details on the data used may be found in the caption to Table 1.

Figure 6 shows that the observed separations agree with $2Z_{\text{peak}}$ for $\sigma/a_{10} \simeq 1-2.5$ in Ophiuchus and Orion, and for $\sigma/a_{10} \simeq 1.5-3.5$ in Taurus. The corresponding ranges computed for $2Z_{\text{min}}$ are $\sigma/a_{10} \simeq 1.5-4$ in Ophiuchus and Orion, and $\sigma/a_{10} \simeq 2-5$ in Taurus. These ranges may now be compared with the observed intercore velocity dispersion σ_{obs} in each region. In Taurus, the range computed according to $2Z_{\text{peak}}$ includes σ_{obs} , while in Ophiuchus and Orion, σ_{obs} lies above the range of theoretical values. On the other hand, the ranges computed for $2Z_{\text{min}}$ include σ_{obs} for all three regions. However, since the physical relevance of Z_{min} is highly uncertain due to unresolved stability issues (§4.3), henceforth we focus on the results for Z_{peak} .

The discrepancy obtained using Z_{peak} can be stated alternatively as follows: given the observed σ and n_s in both Ophiuchus and Orion, the model appears to overestimate $2Z_{\text{obs}}$. These estimates, $2Z_{\text{pred}}$, are given in Table 1 and plotted as open circles in Fig. 6. However, this disagreement may have a rather simple explanation. The model-derived values assume that the parent filament is aligned exactly perpendicular to the line of sight—an unlikely circumstance. Generally, the filament will be inclined at some angle $90^\circ - i$ to the line of sight, so that $2Z_{\text{pred}}$ is reduced to $2Z_{\text{pred}} \cos i$. To bring this into agreement with the mean $2Z_{\text{obs}}$ then requires $i = 50^\circ$ in Ophiuchus and $i = 53^\circ$ in Orion.

An independent measure of the intercore velocity dispersion may be obtained from the observed properties of filaments. According to equation (11) with σ in place of a , the maximum line mass of the parent filament from which the cores could have condensed is:

$$\mu_{\text{max}} = 16.4 \left(\frac{\sigma_{\text{max}}}{a_{10}} \right)^2 \frac{M_{\odot}}{\text{pc}}. \quad (19)$$

Using available observations, we computed an approximate line mass, μ_{obs} , for filaments in Taurus, Ophiuchus, and Orion, with the results given in Table 1. The corresponding σ_{max} , obtained from equation (19) assuming $\mu_{\text{obs}} = \mu_{\text{max}}$, is also tabulated. In Taurus and Ophiuchus, σ_{max} and σ_{obs} are in close agreement, indicating that the filaments themselves are near virial equilibrium. In Orion, σ_{max} should not be compared with σ_{obs} , since the latter is obtained from C^{18}O measurements, whereas μ_{obs} is derived from ^{13}CO observations (Bally et al 1987). Instead, we note that the corresponding linewidth, $\Delta V(^{13}\text{CO}) = 2.2 \text{ kms}^{-1}$, gives a dispersion of $\sigma_{\text{obs}}(^{13}\text{CO}) = 0.97 \text{ kms}^{-1}$, again in very good agreement with σ_{max} .

6. DISCUSSION

If the effect of inclination alone does not account for the above discrepancy between $2Z_{\text{peak}}$ and $2Z_{\text{pred}}$, then this may indicate a more fundamental limitation of the model in its present form. The smaller observed intercore separation (for a given n_s and σ) might be the result of further fragmentation of *stable* cores lying at the low-density end of the equilibrium sequence, Fig. 4. However, the resulting cores would have correspondingly smaller masses than those obtained above in §5, which

are already in only marginal agreement with observations.

Although this paper has not included magnetic effects, it is worth mentioning that, in the presence of a longitudinal magnetic field B that decreases in strength outward from the parent cylinder axis, the critical wavelength for instability is significantly reduced (Nakamura, Hanawa, & Nakano 1993; Hanawa et al 1993). This occurs because the effective sound speed, $c_{\text{eff}} = (a^2 - v_A^2)^{1/2}$, where $v_A \equiv B/(4\pi G\rho)^{1/2}$ is the Alfvén speed, is decreased from its non-magnetic value, thereby reducing thermal support against gravity in the longitudinal direction. If a suitable generalization of the solutions found here exists for magnetized, isothermal cylinders, then the constituent fragments should have a smaller spacing for a given density contrast, perhaps offering more satisfactory agreement with observations.

What is the relation between the intercore spacing and the most unstable and critical wavelengths in the S-O cylinder? We saw in §2 that, in the case of the isothermal layer, it is the *critical* wavelength that determines the inter-filament spacing in S-B’s 2D solution. This feature merits further comment. Let us imagine the temporal growth of an unstable fragment, either filamentary or prolate, to proceed as follows. Fragmentation begins at the scale of λ_{MGR} , the wavelength of the fastest-growing linearly unstable mode of the parental gas distribution. As the fragment (defined as the material residing within the tidal lobe) grows into the nonlinear regime, it begins to attract, and be attracted by, surrounding fragments with the same properties. Thus, the entire chain of masses becomes more tightly bound as a result of the increased gravitational potential energy due to condensation, and the intercore spacing decreases. There is a limit to this process, however, at the scale of λ_{cr} , below which the parent cloud is stable even in the linear regime.

The above conjecture is supported in the planar case by the fact that the gravitational potential energy per unit length per cell increases in absolute value with the amplitude A (S-B 1967). In the cylinder, the same trend is observed in W vs. ρ_c/ρ_s (Fig. 3). Unfortunately, the lack of a 2D analytic solution—and therefore an amplitude—in the cylindrical case precludes the derivation of an algebraic relation between the intercore separation and $\lambda_{z,\text{cr}}$. However, a close inspection of the numerical results suggests that it is again $\lambda_{z,\text{cr}}$ that is of primary importance in filament fragmentation.

Recall from the results of §3.2 that we were able to find 2D equilibria only down to a minimum $Z' \simeq 2.1$, where $\rho_c/\rho_s = 1.2$. Below this value, the method converged to the S-O solution. Now, if the minimum length scale for fragmentation were set by the critical wavelength as in the planar case, then we would expect to find 2D solutions down to a minimum value of $Z' = Z/l_0 = \lambda_{z,\text{cr}}/(2l_0) \simeq 1.97$ (§3.1), with a corresponding $\rho_c/\rho_s \simeq 1$. Our minimum converged value of $Z' = 2.1$ is consistent with this expectation, given the intrinsic inaccuracy of the numerical method. Moreover, the fact that equilibria with $\rho_c/\rho_s > 1.2$ were found for $2.1 \leq Z' \leq 3.91 = \lambda_{z,\text{MGR}}/(2l_0)$ certainly argues *against* any possible significance of $\lambda_{z,\text{MGR}}$ in the final equilibria.

Should a subsequent stability analysis of these solutions reveal that the mass peak in Fig. 4 indeed signifies a stability transition, then an interesting, although highly approximate, criterion for whether a given filament will form stars can be derived. The argument proceeds as follows. The mass peak of Fig. 4 corresponds to $Z_{\text{peak}} = 0.94$, whence $Z_{\text{peak}} = 0.94 l_s = 0.36 (\sigma/a_{10}) \text{ pc}$. Thus, $2Z_{\text{peak}} = 0.72 (\sigma/a_{10}) \text{ pc}$ represents the scale of a single whole fragment formed out of the parent cloud. But what

is the affected region of the original filament? It is likely to be somewhat larger than $2Z_{\text{peak}}$, by the argument summarized in the paragraph above. Roughly speaking, the affected region should be larger by a factor $\sim \lambda_{z,\text{MGR}}/\lambda_{z,\text{cr}} \simeq 2$, since $\lambda_{z,\text{cr}}$ gives the scale at which the filament first becomes unstable to fragmentation (§3.1). Thus, assuming that the original filament was not radially collapsing ($\mu < \mu_{\text{max}}$), we estimate that any filament longer than $\sim 2 \cdot 2Z_{\text{peak}} \simeq 1.44 (\sigma/a_{10})$ pc may be expected to form stars via fragmentation and subsequent dynamical collapse of the prolate fragments. Shorter filaments, which could only harbor cores with $\rho_c/\rho_s < 10$, would require another agent— e.g., an increase in external pressure, ambipolar diffusion, etc.—to initiate collapse.

7. CONCLUSION

We have presented a new family of 2D, numerical solutions of the isothermal Lane-Emden equation in cylindrical symmetry. The equilibria have an embedded, periodic structure, and in this sense are direct counterparts to the 2D solution of

Schmid-Burgk (1967) in planar symmetry. Together, the existence of the two equilibria suggest a fragmentation scheme which seems consistent with the observed hierarchical structure in several well known star-forming regions. Moreover, our results constitute a remarkably simple yet robust explanation for the origin and maintenance of the prolate, gaseous cores that represent the lower rung of this hierarchy. Although we have ignored many physical effects that should be included in subsequent studies (particularly nonthermal motions and magnetic fields), we expect that the shift in emphasis from isolated to embedded structures will prove fruitful in future theoretical work on the origin and evolution of dense cores.

It is a pleasure to thank Steve Stahler for discussions that prompted a search for these solutions. I am grateful to Richard Larson and Dean McLaughlin for useful comments on the manuscript, and to an anonymous referee for suggestions which helped to clarify certain properties of the equilibria.

APPENDIX

RELATION BETWEEN THE SOLUTIONS OF S-B AND S-O

It is worthwhile noting an intriguing correspondence between the solutions of S-B and S-O. Let us examine the structure of one of the cylindrical fragments of §2 in its own right. That is, consider the limit $A \rightarrow 1$, so that $\rho_{0,s} \propto \ell_0^{-1} \rightarrow 0$, giving an isolated cylinder (see equation [4]). Let $\ell_0^{-1} = 2\pi/\lambda_{x,\text{cr}} \equiv k_{x,\text{cr}}$. Then in the limit $k_{x,\text{cr}} \rightarrow 0$ the solution (3) becomes

$$\rho(x, y) = \rho_c \left[1 - \frac{Ax^2 + y^2}{1-A} k_{x,\text{cr}}^2 + O(k_{x,\text{cr}}^4) \right]. \quad (\text{A1})$$

In terms of $k_{x,\text{cr}}$, equation (8) reads

$$k_{x,\text{cr}}^2 \ell_c^2 = \frac{1-A}{1+A},$$

the substitution of which into equation (A1) gives

$$\begin{aligned} \rho(x, y) &= \rho_c \left[1 - \frac{Ax^2 + y^2}{\ell_c^2 (1+A)} + O(k_{x,\text{cr}}^4) \right] \\ &= \rho_c \left[1 - \frac{r^2}{2 \ell_c^2} + O(k_{x,\text{cr}}^4) \right], \end{aligned} \quad (\text{A2})$$

in the limit as $A \rightarrow 1$, where we have noted that $r^2 = x^2 + y^2$, appropriate to the geometry of the isolated cylindrical fragment.

The S-O solution, on the other hand, reduces to the following in the limit of small r (equation [10]):

$$\rho(r, z) = \rho_{0,f} \left[1 - \frac{2 r^2}{l_0^2} + O(r^4) \right]. \quad (\text{A3})$$

Equations (A2) and (A3) are identical, at order r^2 , provided that: (i) $l_0^2 = 4\ell_c^2$; and (ii) $\rho_{0,f} = \rho_c$. Recalling the definitions of ℓ_c and l_0 given in §2 and 3, if the latter is true, then so is the former. But equality (ii) does indeed hold, since the planar fragment has a topology indistinguishable from that of a cylinder in the prescribed limit. Thus, the S-O solution appears as the unique $A \rightarrow 1$ limit of the S-B solution.

REFERENCES

- Alves, J., Lada, C.J., Lada, E.A., Kenyon, S.J., & Phelps, R., 1998, *ApJ*, 506, 292
- Bally, J., Langer, W.D., Stark, A.A., & Wilson, R.W. 1987, *ApJ*, 312, L45
- Cesaroni, R., & Wilson, T.J. 1994, *A&A*, 281, 209
- Chandrasekhar, S. 1958, *An Introduction to the Study of Stellar Structure* (New York: Dover)
- Curry, C.L., & Stahler, S.W. 2000, in preparation
- David, M., & Verschueren, W. 1987, *A&A*, 186, 295
- Dutrey, A., Langer, W.D., Bally, J., Duvert, G., Castets, A., & Wilson, R.W. 1991, *A&A*, 247, L9
- Dutrey, A., Duvert, G., Castets, A., Langer, W.D., Bally, J., & Wilson, R.W. 1993, *A&A*, 270, 468
- Elmegreen, B.G., & Elmegreen, D.M. 1978, *ApJ*, 220, 1051
- Fiedler, R.A., & Mouschovias, T.Ch. 1992, *ApJ*, 391, 199
- Fiege, J., & Pudritz, R.E. 2000*a*, *MNRAS*, 311, 105
- Fiege, J., & Pudritz, R.E. 2000*b*, *ApJ*, in press
- Fleischer, J. 1998, *Physica Scripta*, T74, 86
- Gaida, M., Ungerechts, H., & Winnewisser, G. 1984, *A&A*, 137, 17
- Hanawa, T., et al 1993, *ApJ*, 404, L83
- Heyer, M.H., Vrba, F.J., Snell, R.L., Schloerb, F.P., Strom, S.E., Goldsmith, P.F., & Strom, K.M. 1987, *ApJ*, 321, 855
- Inutsuka, S., & Miyama, S.M. 1992, *ApJ*, 388, 392
- Inutsuka, S., & Miyama, S.M. 1997, *ApJ*, 480, 681
- Jijina, J., Myers, P.C., & Adams, F.C. 1999, *ApJS*, 125, 161
- Johnstone, D., & Bally, J. 1999, *ApJ*, 510, L49
- Kulkarni, S.R., & Heiles, C. 1988, in *Galactic and Extragalactic Radio Astronomy*, ed. G.L. Verschuur & K.I. Kellermann (Berlin: Springer-Verlag), 95
- Lada, C.J., Alves, J., & Lada, E.A. 1999, *ApJ*, 512, 250
- Larson, R.B. 1985, *MNRAS*, 214, 379
- Ledoux, P. 1951, *Ann. d'Ap.*, 14, 438
- Lizano, S., & Shu, F.H. 1989, *ApJ*, 342, 834
- Loren, R.B. 1989, *ApJ*, 338, 902
- McCray, R., & Kafatos, M. 1987, *ApJ*, 317, 190
- McKee, C.F., Zweibel, E.G., Goodman, A.A., & Heiles, C. 1993, in *Protostars and Planets III*, ed. E.H. Levy & J.I. Lunine (Tucson: University of Arizona Press), 327
- Miyama, S.M., Narita, S., & Hayashi, C. 1987*a*, *Prog. Theor. Phys.*, 78, 1051
- Miyama, S.M., Narita, S., & Hayashi, C. 1987*b*, *Prog. Theor. Phys.*, 78, 1273
- Myers, P.C., Fuller, G.A., Goodman, A.A., & Benson, P.J. 1991, *ApJ*, 376, 561
- Nagai, T., Inutsuka, S., & Miyama, S.M. 1998, *ApJ*, 506, 306
- Nagasawa, M. 1987, *Prog. Theor. Phys.*, 77, 635
- Nakamura, F., Hanawa, T., & Nakano, T. 1993, *PASJ*, 45, 551
- Nercessian, E., Castets, A., Benayoun, J.J., Cernicharo, J. 1988, *A&A*, 189, 207
- Nozawa, S., Mizuno, A., Teshima, Y., Ogawa, H., & Fukui, Y. 1991, *ApJS*, 77, 647
- Onishi, T., Mizuno, A., Kawamura, A., Ogawa, H., & Fukui, Y. 1996, *ApJ*, 465, 815
- Onishi, T., Mizuno, A., Kawamura, A., Ogawa, H., & Fukui, Y. 1998, *ApJ*, 502, 296
- Ostriker, J. 1964, *ApJ*, 140, 1056
- Roberts, W.W. 1969, *ApJ*, 158, 123
- Ryden, B.S. 1996, *ApJ*, 471, 822
- Scalo, J.M. 1985, in *Protostars and Planets II*, ed. D. Black & M.S. Matthews (Tucson: University of Arizona Press), 201
- Schmid-Burgk, J. 1967, *ApJ*, 149, 727
- Schneider, S., & Elmegreen, B.G. 1979, *ApJS*, 41, 87
- Smith, J. 1980, *ApJ* 238, 842
- Spitzer, L., Jr. 1942, *ApJ* 95, 329
- Stodolkiewicz, J.S. 1963, *Acta Astron.*, 13, 30
- Stuart, J.T., 1967, *J. Fluid Mech.*, 29, 417
- Tachihara, K., Mizuno, A., & Fukui, Y. 2000, *ApJ*, 528, 817
- Tassoul, J.-L. 1978, *Theory of Rotating Stars* (Princeton: Princeton University Press)
- Tatematsu, K., et al 1993, *ApJ*, 404, 643

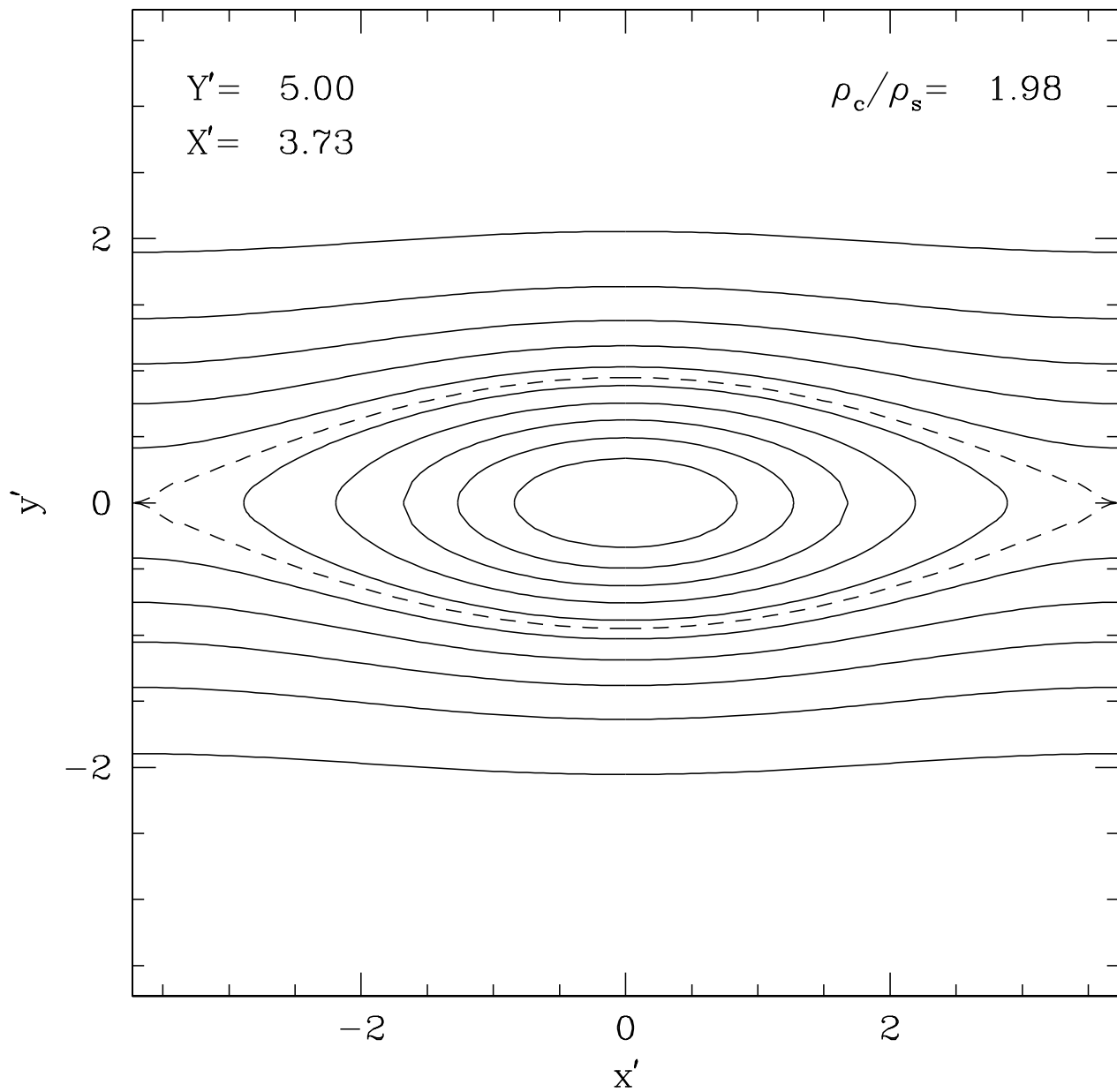


FIG. 1.— The closest numerical equivalent to S-B's $A = 0.17$ solution. Solid curves are equidensity contours, linearly spaced in ρ from $\rho(0,0)/\rho_s = 1.98$ down to $\rho/\rho_s = 0.18$. The dashed curve indicates the surface $\rho = \rho_s$. Recall that $x' \equiv x/\ell_c, \dots$ etc.

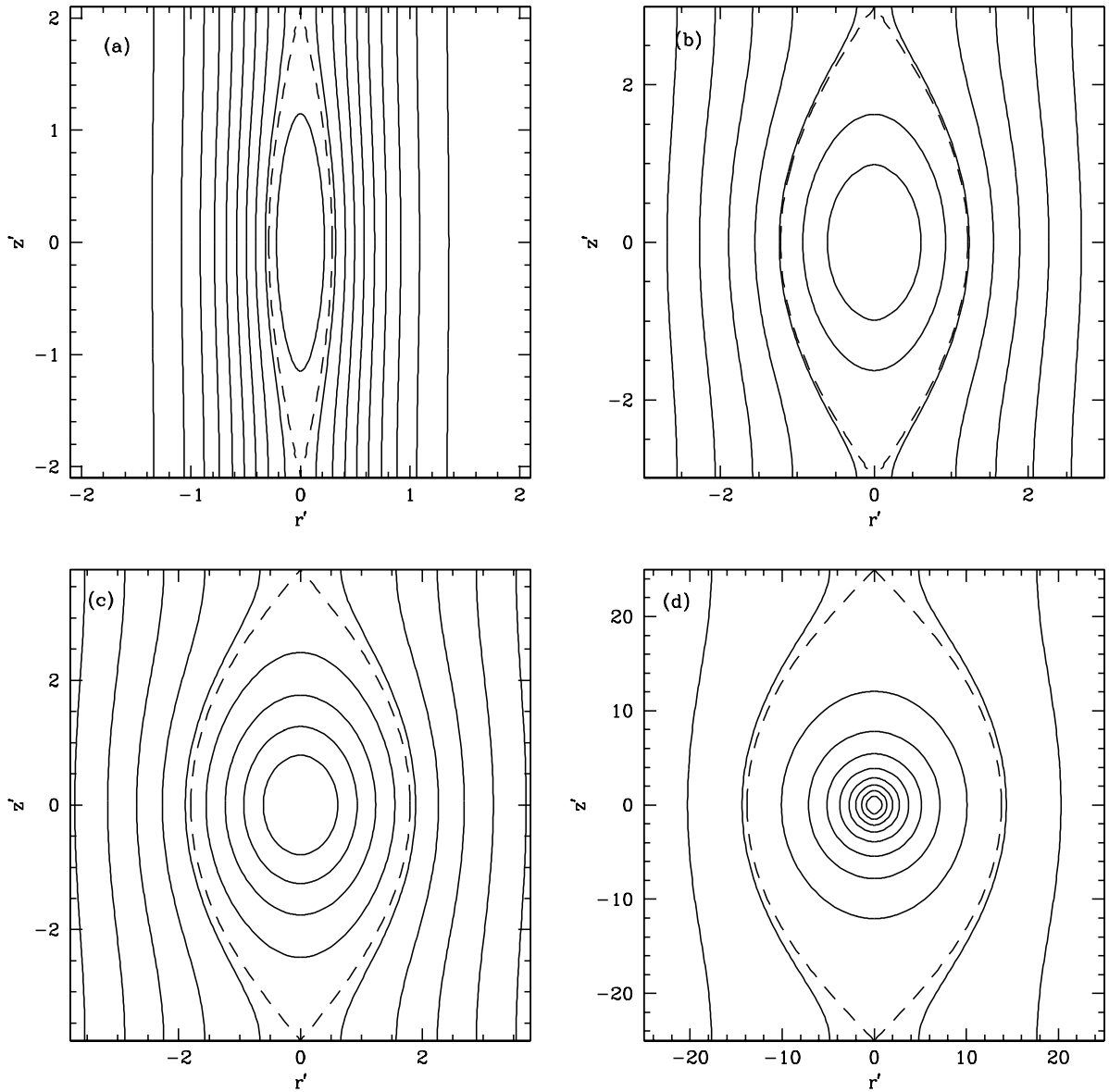


FIG. 2.— Four embedded cores in the isothermal filament. Each is characterized by its value of (Z', R') : (a) (2.1, 2.1); (b) (3.0, 5.0); (c) (3.79, 5.0); (d) (25.0, 28.0). The corresponding density contrasts, ρ_c/ρ_s , are 1.17, 4.70, 10.49, and 1076, respectively. Contours are spaced linearly in (a), logarithmically in (b), (c), and (d). Recall that $r' \equiv r/l_c, \dots$ etc.

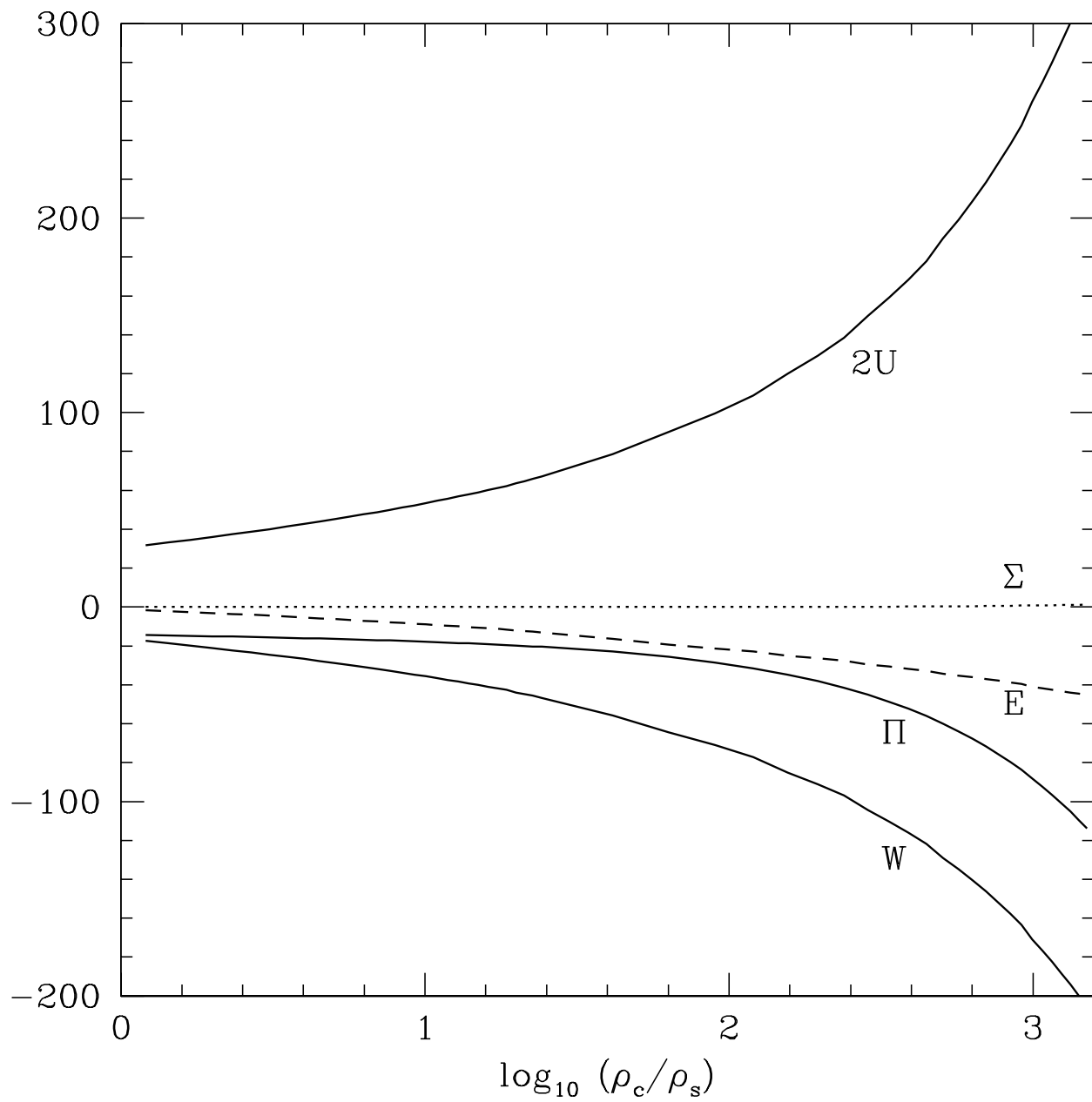


FIG. 3.— Solid curves represent individual terms of the virial theorem for an entire cell, plotted against core density contrast (center to tidal lobe). The dotted curve is the sum of these terms, while the dashed curve is the total energy. See §4.1 for details.

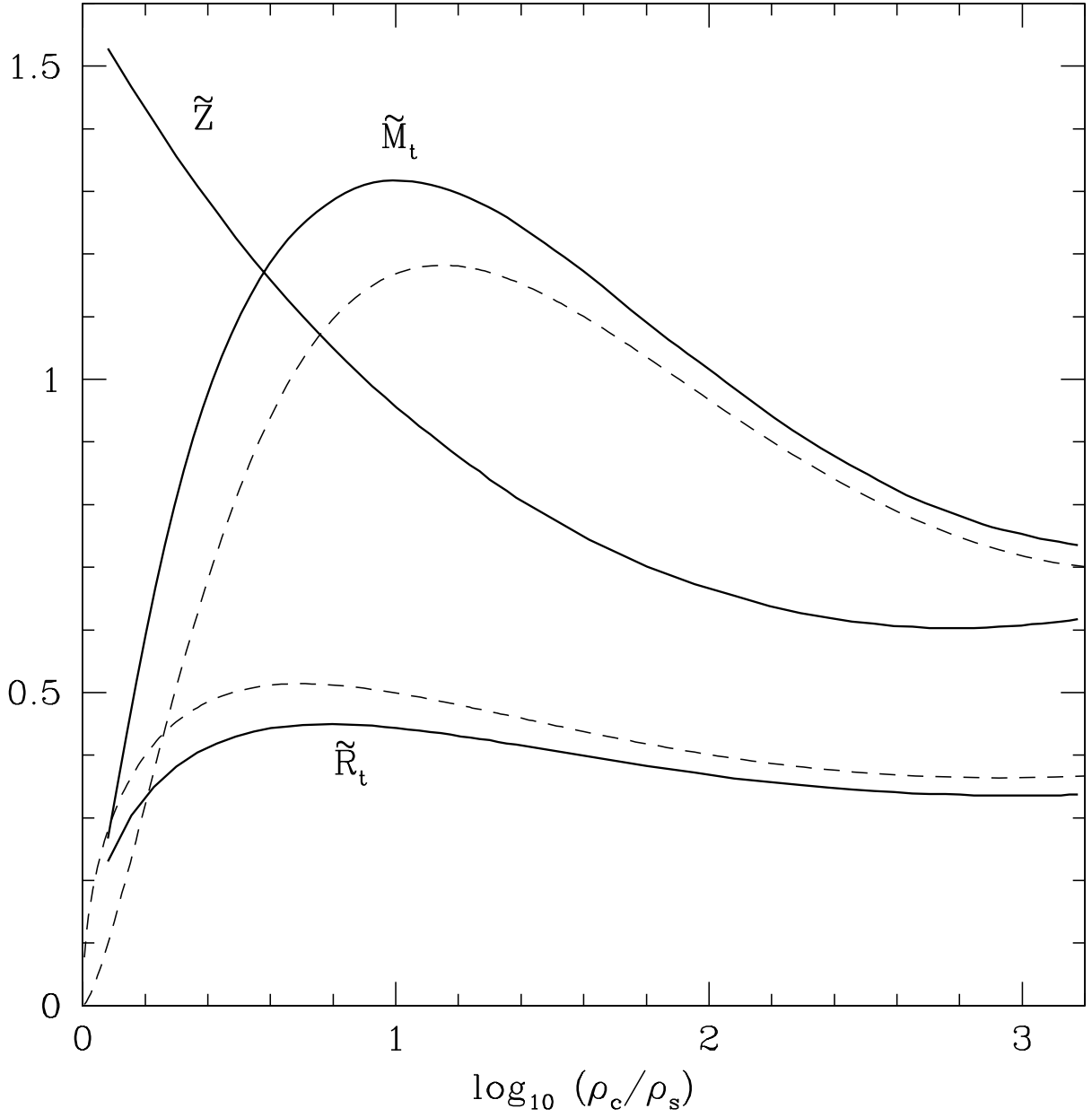


FIG. 4.— Solid curves show the entire sequence of models that were calculated, represented as \tilde{Z} , \tilde{R}_t , and \tilde{M}_t vs. central concentration, ρ_c/ρ_s . The overall behavior is similar to that of the B-E sequence, shown by dashed lines (dimensionless mass, top; dimensionless radius, bottom). See text for details.

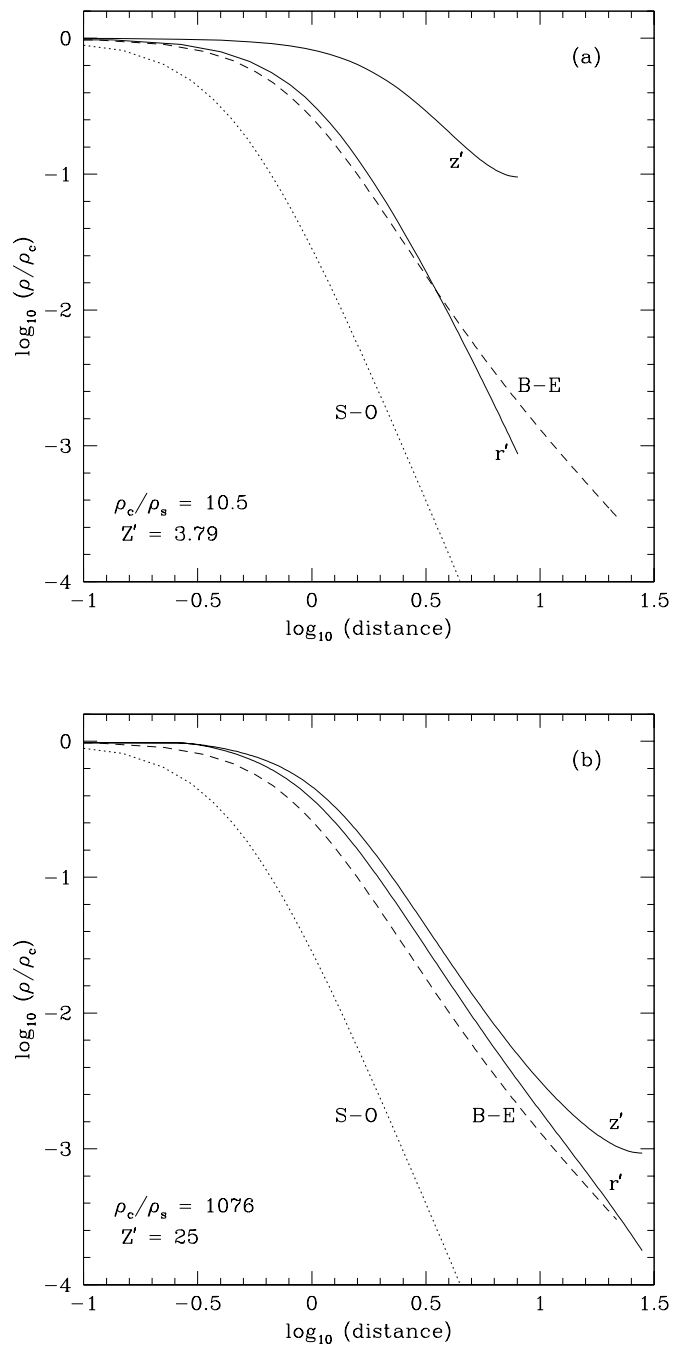


FIG. 5.— (a) Density profiles along the polar (z') and equatorial (r') axes of the equilibrium depicted in (c) of Fig. 2. Also shown are the radial profiles of a S-O cylinder (dotted curve) and a B-E sphere (dashed curve). (b) Same as (a), for the equilibrium depicted in Fig. 2 (d).

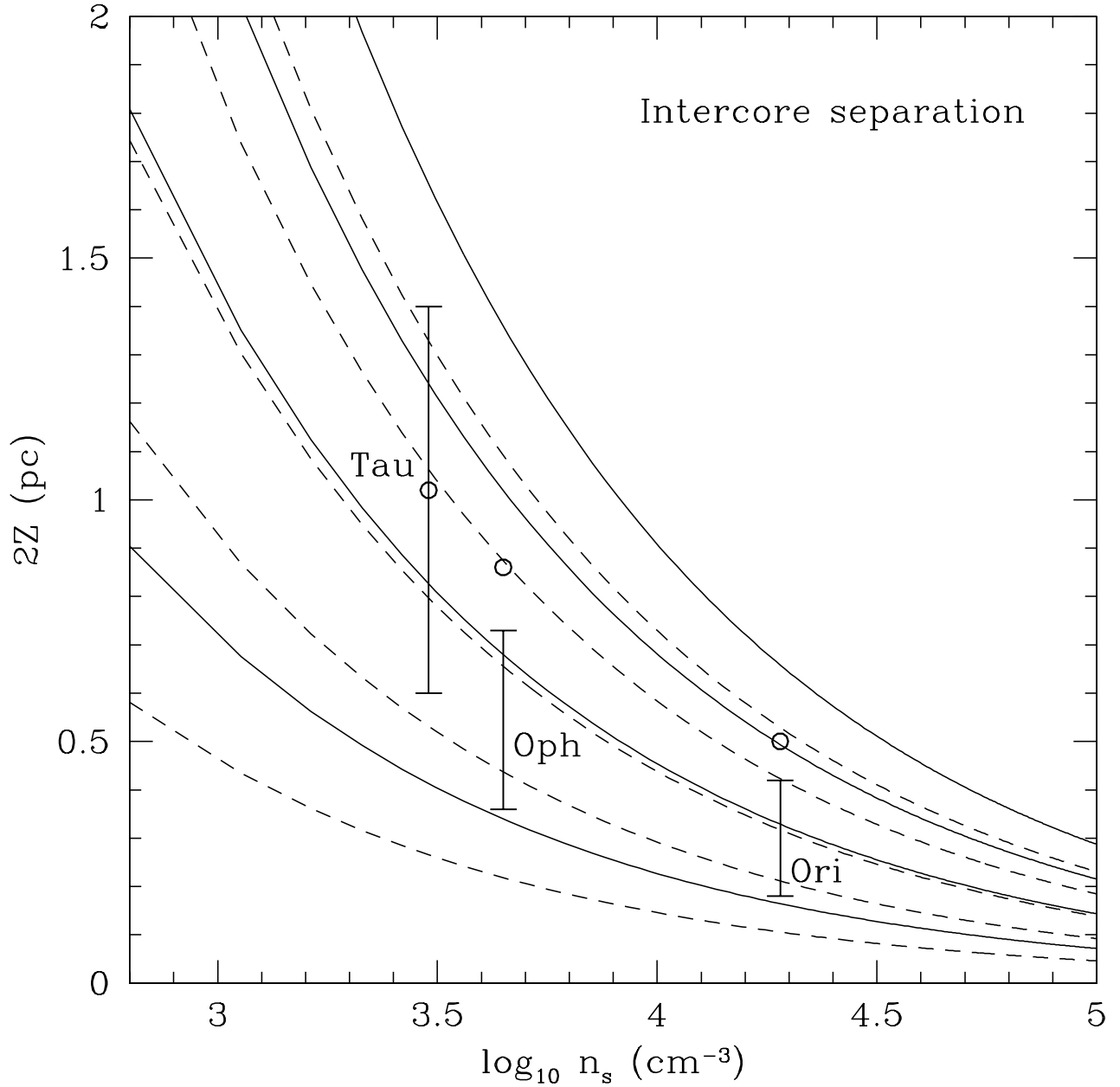


FIG. 6.— Intercore separation, $2Z$, as a function of n_s . Solid curves are $2Z_{\text{peak}}$; from bottom to top, $\sigma/a_{10} = 1, 2, 3$ and 4 , respectively. Dashed curves are $2Z_{\text{min}}$; from bottom to top, $\sigma/a_{10} = 1, 2, 3, 4$ and 5 , respectively. Vertical segments indicate approximate ranges of $2Z$ observed in three regions: from left to right, Taurus, Ophiuchus, and Orion. Open circles are predicted values of $2Z$, assuming no inclination of the filament to the line of sight. See Table 1 and text for details.

TABLE 1: MEAN PROPERTIES OF SELECTED FILAMENTS IN TAURUS, OPHIUCHUS, AND ORION.

Region, Cloud	μ_{obs} (M_{\odot}/pc)	$\log_{10} n_{s,\text{obs}}$ (cm^{-3})	σ_{obs} (km s^{-1})	$2Z_{\text{obs}}$ (pc)	$2Z_{\text{pred}}$ (pc)	σ_{max}	Refs. (km s^{-1})
Taurus, L1495	100	3.48	0.47	0.6—1.4	1.02	0.47	1; 2; 3; 4
Ophiuchus, L204	110	3.65	0.48	0.36—0.73	0.86	0.49	5; 5; 5; 6
Orion, L1641	385	4.28	0.58	0.18—0.42	0.50	0.92	7; 8; 8; 9

NOTE.— The filaments in each region were chosen on the basis of their large apparent axial ratios (length, $L/\text{width} \gtrsim 20$) as observed in ^{13}CO maps, from which both M and L , and thus μ , were deduced. The intercore separations, $2Z_{\text{obs}}$, are nearest core distances derived from C^{18}O maps in Taurus and Ophiuchus and NH_3 maps in Orion. The mean intercore density, $n_{s,\text{obs}}$, is the density corresponding to the mean $2Z_{\text{obs}}$ in each region. This requires results from the appropriate (scale-dependent) molecular tracer: ^{13}CO in Taurus and Ophiuchus, and C^{18}O in Orion. The velocity dispersion, σ_{obs} , is chosen in the same manner. References to the literature are ordered as follows. The first reference in each row is the source of μ_{obs} , followed by references to the sources of $n_{s,\text{obs}}$, σ_{obs} , and $2Z_{\text{obs}}$, each separated by a semicolon.

REFERENCES.—(1) Gaida et al 1984; (2) Mizuno et al 1995; (3) Nercessian et al 1988; (4) Onishi et al 1996; (5) Nozawa et al 1991; (6) Tachihara et al 2000; (7) Bally et al 1987; (8) Dutrey et al 1993; (9) Cesaroni & Wilson 1994.